Nano Energy 118 (2023) 108936

Contents lists available at ScienceDirect

Nano Energy

journal homepage: www.elsevier.com/locate/nanoen

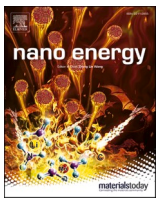

Flexible solid-state Zn-Co MOFs@MXene supercapacitors and organic ion hydrogel sensors for self-powered smart sensing applications

Guo-Tao Xiang [a], Na Chen [a], Bin Lu [a], Jia-Lei Xu [a], Raul D. Rodriguez [b], Evgeniya Sheremet [b], Yong-Da Hu [c], Jin-Ju Chen [a,*]

[a] School of Materials and Energy, University of Electronic Science and Technology of China, Chengdu 610054, PR China
[b] Tomsk Polytechnic University, Lenin Ave. 30, 634050 Tomsk, Russia
[c] School of Integrated Circuit Science and Engineering (Exemplary School of Microelectronics), University of Electronic Science and Technology of China, Chengdu 610054, PR China

ARTICLE INFO

Keywords:
Self-powered
Supercapacitor
Sensor
Hydrogel

ABSTRACT

Stable and continuous detection of physiological signals without an external power supply is a crucial technology to realize wearable electronics as the next generation of flexible electronic devices. In this work, a self-powered smart system with flexible solid-state Zn-Co MOFs@MXene supercapacitors and polyacrylamide-$BaTiO_3$/NaCl (PAM-BTO/NaCl) organic ionic hydrogel sensors are designed. The supercapacitor demonstrates a high energy density of 51 Wh/kg at a power density of 1.59 kW/kg. In particular, it maintains exceptional mechanical flexibility under different bending environments. The resistance change rate of the organic ionic hydrogel sensor exhibits a linear response within the strain range of 0–400 % and 400–600 %, respectively, and it shows outstanding electromechanical stability with almost unchanged performance under multiple identical tensile strains. Furthermore, the self-powered integrated system can be conveniently used for real-time detection of human motion and small strains. These findings highlight the unlimited application potential of self-powered integrated system in wearable devices.

1. Introduction

Lately, wearable electronic devices and "e-skins" are becoming important players in personal health and quality of life technologies. They offer high level of integration, versatility, and comfort, leading to the widespread use of stretch-based sensing electronics [1–3]. As a result, flexible/stretchable integrated systems have recently developed rapidly, among which self-powered integrated sensing systems are gradually becoming a promising strategic direction in wearable electronics [4,5]. An integrated energy storage device can independently power sensors without relying on an external power source [6,7]. For wearable applications, strain sensors play a crucial role in converting mechanical deformations into electronic signals. To integrate these sensors effectively, energy storage devices such as supercapacitors are required [8–11]. However, the current limitations associated with rigid materials and structural designs often result it poor flexibility and limited sensing capabilities in integrated systems [12,13]. Consequently, there is a fundamental need to develop new materials that offer exceptional stretchability, high sensitivity, and reliability to meet the demands of wearable electronic devices [14].

Flexible solid-state supercapacitors store charge through highly reversible bilayer ion adsorption and/or fast Faraday redox reactions [15–17]. These supercapacitors offer numerous advantages, such as high capacity, fast charge and discharge rates, and environmental friendliness. As a result, they serve as ideal energy storage alternatives for portable electronic devices that require fast energy capture and delivery [18–20]. Notably, solid-state supercapacitors exhibit superior safety compared to water-based capacitors, as they remain stable even under significant mechanical deformations without the risk of electrolyte leakage [21,22]. Hydrogels are considered potential materials for the fabrication of flexible supercapacitors due to their excellent mechanical properties and ionic conductivity [23]. For example, Zhu et al.[10] prepared flexible self-healing polyvinyl alcohol hydrogel (B-PVA/KCl) substrates by combining physical and chemical cross-linking. The prepared supercapacitor showed good capacitive performance and excellent mechanical properties, with a capacitance retention rate of over 90 % during 1000 tensile and 1500 bending cycles, as well as good self-healing properties. The PVA-based hydrogel showed excellent

* Corresponding author.
E-mail address: jinjuchen@uestc.edu.cn (J.-J. Chen).

https://doi.org/10.1016/j.nanoen.2023.108936
Received 5 August 2023; Received in revised form 22 September 2023; Accepted 25 September 2023
Available online 27 September 2023

flexibility, establishing its potential for practical applications in smart energy systems. In their study, Wang et al. [24]. reported a wearable multifunctional sensor featuring an integrated micro-capacitor array. The results showed the direct applicability of the integrated system in monitoring the biophysical signals of the human body. This successful integration of multifunctional sensors with supercapacitors perfectly demonstrates the feasibility and offers robust evidence for the development of wearable integrated systems. The ionic conductive hydrogel is a typical solvated viscoelastic flexible polymer network that possesses a remarkable ability to absorb a significant amount of water. This hydrogel material exhibits exceptional properties such as high sensitivity, long durability, and excellent wearability, making it highly suitable for human strain detection and positioning it as a promising material for sensor applications [25,26]. For example, Huang et al. [7]. successfully developed a double reticulated ionic hydrogel by incorporating NaCl and glycerol (Gly) into poly (vinyl alcohol)/bene (amido-acrylic acid) (PVA/PAMAA). This innovative hydrogel exhibited frost resistance, self-healing, adhesion, and toughness. Based on this material, strain sensors, and flexible all-solid-state supercapacitors were individually assembled. The resulting strain sensors exhibited precise and reliable detection of various mechanical deformations. Additionally, the flexible all-solid-state supercapacitor showcased a specific capacitance of 75.75 mF cm^{-2} and demonstrated excellent cycling stability. These findings demonstrate the effectiveness of the ion-conductive hydrogel as it provides an ion transport pathway, enhancing electrical conductivity in the assembled devices.

Until now, there has been limited research in energy storage-sensing integrated systems [27–29]. The fabrication of these integrated sensors and capacitors requires optimizing various properties in each device unit. This includes ensuring the flexible stability of supercapacitors, attaining a large specific capacity, enabling easy liquid-electrolyte-free packaging, as well as the high sensitivity and high tensile strain in sensors. Therefore, designing integrated energy-independent sensing systems with excellent overall performance remains a considerable challenge.

In this work, we developed a self-powered sensing system by integrating a Zn-Co MOFs@MXene flexible solid-state supercapacitor and a polyacrylamide-$BaTiO_3$/NaCl (PAM-BTO/NaCl) organic ionic hydrogel sensor. The fabricated supercapacitors have excellent capacitance performance, reaching up to 144.7 F/g at 1 A/g current density and excellent cycling stability. Moreover, they exhibited impressive mechanical properties, maintaining nearly constant capacitance even during multiple stretching and bending at different angles. The flexible PAM-BTO/NaCl hydrogel strain sensors exhibited outstanding sensing performance characterized by high sensitivity, ductility, and electromechanical stability even after undergoing high-strength bending. These integrated sensing systems could be seamlessly attached to the human epidermis. Driven by capacitive power, the strain sensor successfully detected the full range of human motion.

2. Results and discussion

Fig. 1a illustrates the synthetic process of Zn-Co MOFs@MXene. The MXene nanosheets were synthesized by selectively etching the metallic Al layer in Ti_3AlC_2. The resulting MXene nanosheets, exfoliated by dimethyl sulphoxide (DMSO), shows flat and smooth surfaces. These nanosheets provide abundant interlayer functional groups that promoted ligand deprotonation. Furthermore, the exfoliated lamellar structure has a significantly increased specific surface area and a significant number of active sites, which accelerate the in-situ growth of amorphous MOFs. Through electrostatic interactions, positively charged cobalt and zinc ions were attracted to the electronegative functional groups (such as -O, -OH and -F) on the surface of MXene. This attraction led to the self-assembly of Zn-Co MOFs@MXene upon adding 2-methylimidazole. In this structure, MXene acts as a conductive support, which not only realizes fast electron and ion transport but also prevents the aggregation and volume expansion of Zn-Co MOFs during redox processes. In turn, the Zn-Co MOFs can act as spacers to separate the MXene nanosheets and prevent restacking, creating a "pillar effect" that enlarges the interlayer spacing of the MXene layers, which further facilitates ion diffusion and improves the stability of the layered structure. Fig. 1b illustrates the synthesis process of the PAM-BTO/NaCl organo-ionic hydrogel. The hydrogels were prepared using a free-radical polymerization strategy, resulting in three-dimensional porous structures. Polyacrylamide (PAM) was synthesized through the free radical polymerization of acrylamide (AM) monomer using N, N′-methylene bis (acrylamide) as the chemical cross-linker and ammonium persulfate (APS) as the initiator. The reaction was catalyzed by tetramethylethylenediamine (TEMED). During the polymerization process, hydroxyl and amide groups formed hydrogen bonds, leading to the formation of a

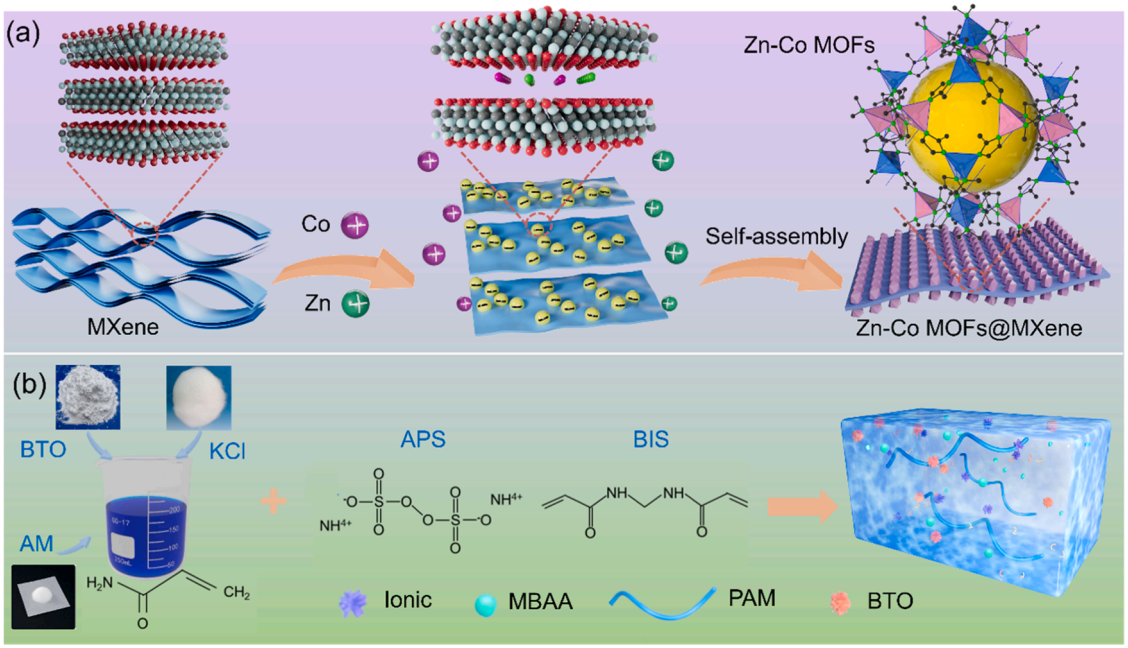

Fig. 1. Schematic diagram of the synthesis process of (a) Zn-Co MOFs@MXene and (b) organic ionic hydrogels.

solid physical cross-linked network through the rearrangement of macromolecular chains. To enhance the sensitivity of the hydrogel, barium titanate (BTO) was directly added as a functional material and uniformly distributed in the hydrogel matrix. Furthermore, the addition of NaCl produced a salting effect, which enhanced electrostatic interactions contributing to the overall toughness of the hydrogel.

Fig. S1 and Fig. 2a show the scanning electron microscopy (SEM) images of MXene nanosheets before and after undergoing ultrasonic exfoliation, respectively. In Fig. S1, a clear accumulation between the layers is observed. However, in Fig. 2a, after exfoliation, the accordion-like structure of the few-layer MXene becomes clearly visible. The addition of DMSO as a functional agent aids in disrupting the hydrogen bonds and van der Waals forces between the layers, facilitating their separation. As a result, the few-layer MXene configuration is achieved, allowing for a more extensive exposure of electrochemically active surfaces to the electrolyte.[30] In addition, the few-layer MXene exhibits good hydrophilicity and large specific surface area, facilitating reactions in aqueous solutions and enabling the construction of three-dimensional structures. Fig. 2b illustrates the smooth surface cubic morphology of the nanoscale Zn-Co MOFs particles obtained through the combined action of a surfactant and an excess of dimethylimidazole. In Fig. 2c, the morphological characteristics of Zn-Co MOFs and few-layer MXene complexes are shown, revealing a roughened surface on the layered structure, indicating their successful integration. Their synergistic effect is expected to enhance the electrochemical properties of the composite material. The ultrasonic treatment effectively exfoliated the multilayer Ti_3C_2 bulk, resulting in the production of well-separated fewer-layer MXene nanosheets. This successful exfoliation is further confirmed by the transmission electron microscopy (TEM) image shown in Fig. 2d. Fig. 2e shows a more detailed view of the Zn-Co MOFs@MXene morphology, revealing a composite structure consisting of particles and lamellae. It is evident that the polyhedral particles of Zn-Co MOFs are loaded onto the MXene surface. High-resolution TEM images depicted in Fig. 2f show lattice spacings of 0.268 and 0.186 nm, corresponding to the (111) plane of Zn-Co MOFs and the (002) plane of MXene, respectively. The selected area electron diffraction (SAED) images in Fig. 2g show concentric diffraction rings indicating the presence of Zn-Co MOFs and MXene crystals. The concentric diffraction rings are assigned to Zn-Co MOFs corresponding to the (201) and (132) crystal planes, and the (011) crystal plane of MXene. Energy dispersive spectroscopy (EDS) (Fig. S2) and elemental mapping analysis in Fig. 2h indicate that Ti, C, Co, and Zn elements are uniformly distributed throughout the lamellar structure, further confirming the coexistence of Zn-Co in the MXene lamellar matrix.

In the case of ionic hydrogels (as depicted in Fig. 3a), a notable difference can be observed between oven-dried PAM-BTO/NaCl gels (Fig. 3d), which lack pore structures, and lyophilized PAM-BTO/NaCl gels (Fig. 3b) that show significant porous characteristics on both the surface and interior. These porous structures play an important rule facilitating the entry of solvent molecules and salt ions. The fractured surface of the hydrogel (Fig. 3c) displays a network structure with irregular interconnections. Pores of different depths and sizes are arranged in a disorderly manner. Generally, shallower holes tend to have larger diameters, while deeper pores have smaller diameters. This arrangement of micropores helps to prevent stress concentration and allows for the absorption of a large number of free ions, ultimately

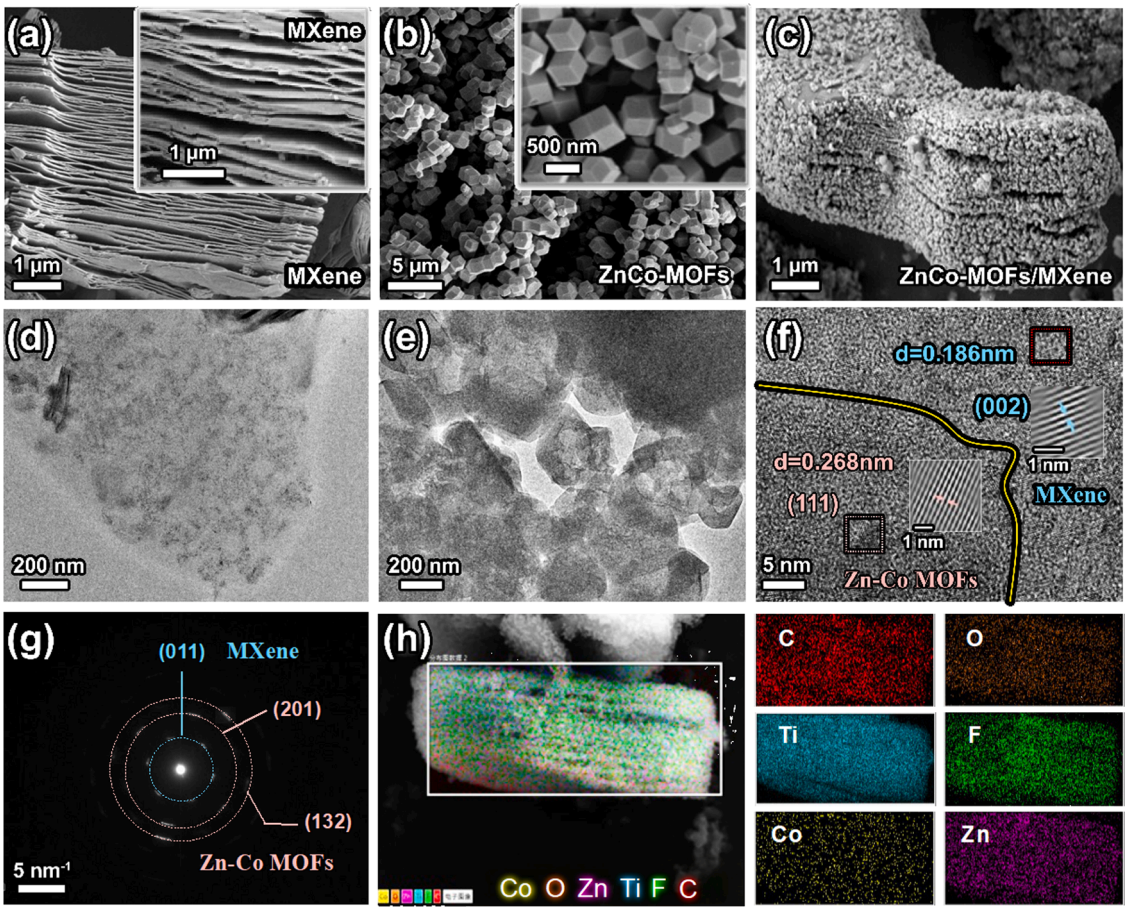

Fig. 2. SEM images of (a) MXene, (b) Zn-Co MOFs, and (c) Zn-Co MOFs@MXene; (d) TEM image of MXene, (e) TEM image, (f) HRTEM image, (g)SAED diffraction pattern, and (h) High-angle annular dark field-scanning transmission electron microscopy (HAADF-STEM) image and the corresponding EDS elemental mapping of Zn-Co MOFs@MXene.

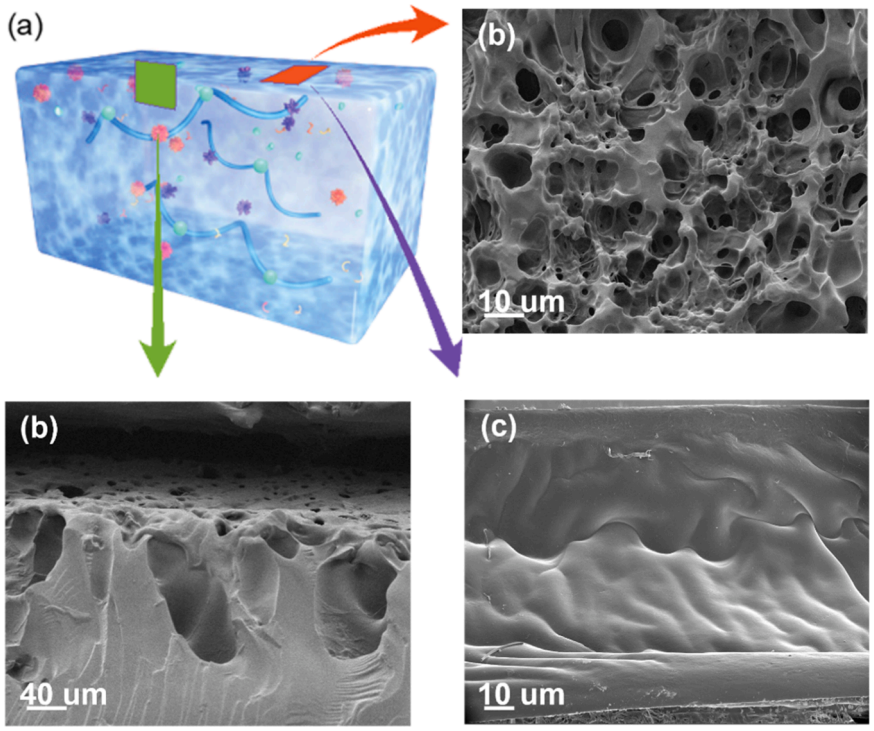

Fig. 3. (a) Sketch of the PAM-BTO/NaCl sample indicating the different directions SEM imaging was obtained. (b) Top view. (c) Cross-section side view. (d) Cross-section side view of an oven-dried sample.

benefiting the overall hydrogel properties [31].

X-ray photoelectron spectroscopy (XPS) analysis was carried out to investigate the surface elemental composition and chemical valence of the Zn-Co MOFs@MXene samples. The broad-sweep spectrum (Fig. S3) confirmed the presence of Zn, Co, Ti, C, and O in the composites. The Zn XPS spectrum in Fig. 4a exhibited two main peaks at 1021.5 and

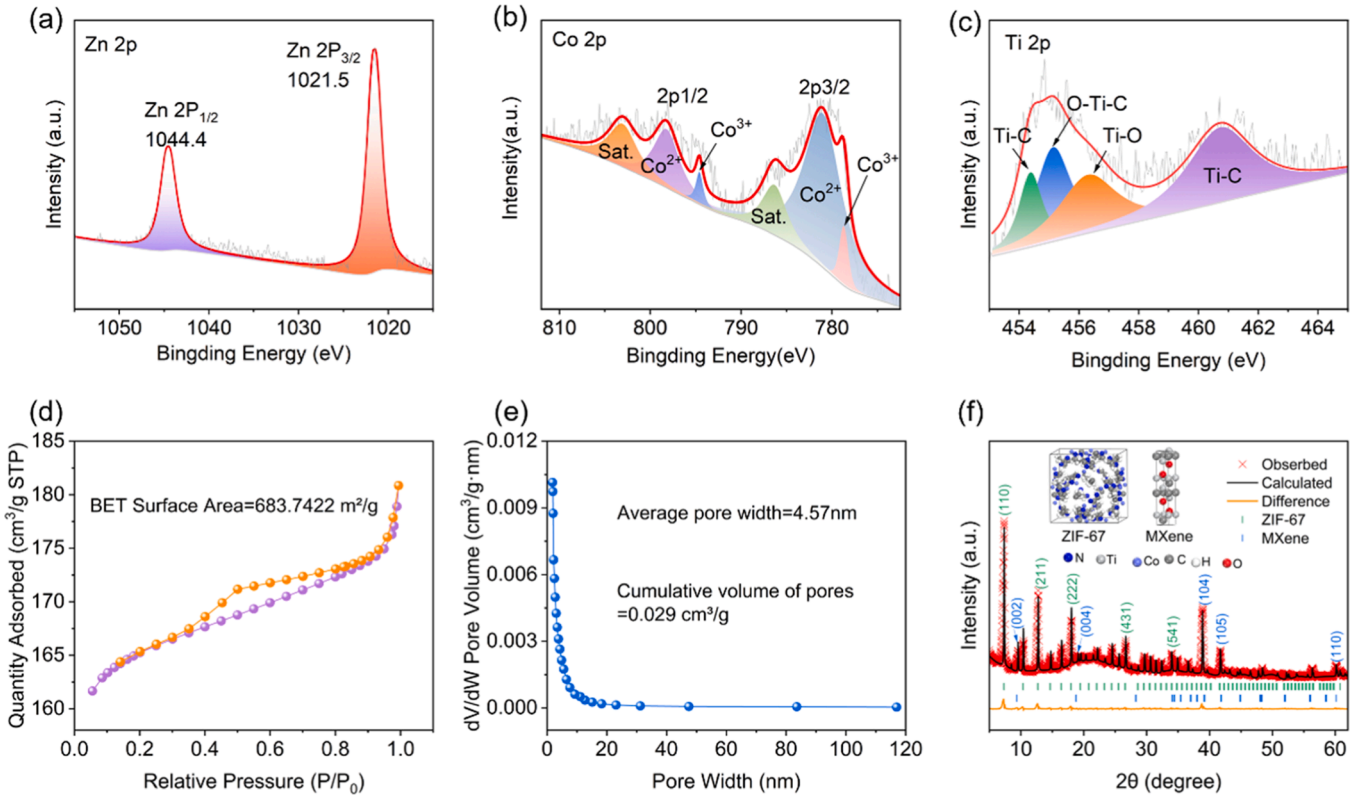

Fig. 4. High-resolution XPS spectra of (a) Zn 2p, (b) Co 2p, (c) Ti 2p. (d) N_2 adsorption–desorption isotherm and (e) the pore size distribution of Zn-Co MOFs@MXene. (f) XRD profiles and fit of the Rietveld refinement of Zn-Co MOFs@MXene.

1044.4 eV, corresponding to the Zn $2p_{3/2}$ and $2p_{1/2}$ regions, respectively [32]. Fig. 4b showed peaks at binding energies of 778.3 and 781.3 eV, belonging to the Co $2p_{3/2}$ of Co^{3+} and Co^{2+} species, respectively. Additionally, the peaks at binding energies of 794.5 and 797.1 eV are characteristic of Co $2p_{1/2}$ of Co^{3+} and Co^{2+}, respectively. The Co 2p peak could also be deconvoluted into two satellite peaks at 787.6 and 804.5 eV [33,34]. In Fig. 4c, a prominent XPS peak on the right belongs to the Ti-C bond inherent in the Ti 2p region. On the left, the XPS peak is divided into Ti-O, O-Ti-C, and Ti-C bonds, indicating the formation of new bonds mainly due to the interaction between surface groups and titanium [35,36]. The O 1 s spectrum (Fig. S4a) exhibits four peaks representing Ti-O, C-Ti-O_x, C-O, and C═O. The C═O and C-O orbitals originate from organic ligands and oxygen-containing functional groups present on the $Ti_3C_2T_x$ surface, while the Ti-O peak traces the oxidation process of MXene [37]. The local spectrum of C1s in Fig. S4b reveals the chemical bonding involving carbon, which mainly arises from the organic ligands synthesized by MOF and $Ti_3C_2T_x$ [38]. The specific surface area can visualize the contact area between the electrode and the electrolyte, while the pore size distribution plays a key role in ion transfer. Therefore, the specific surface area and pore size distribution are particularly important for electrochemistry. The N_2 adsorption-desorption isotherm of Zn-Co MOFs@MXene display H_3 hysteresis loop and typical IV equilibrium isotherm (Fig. 4d) with a large BET specific surface area of 683.742 m^2/g. The reasons for the large BET surface area of Zn-Co MOFs@MXene can be attributed to two aspects: (1) the MXene nanosheets limit the accumulation and agglomeration of Zn-Co MOFs; (2) the Zn-Co MOFs nanoparticles within the MXene interlayer prevent the buildup of the MXene nanosheets, which maintains the laminar structure. Fig. 4e further shows that Zn-Co MOFs@MXene presents average pore size distributions (4.57 nm) and cumulative volume of pores (0.029 cm^3/g), which can guarantee a reliable electrochemical reaction for the ion transfer. Compared with recently reported work (Table S1), Zn-Co MOFs@MXene exhibits the largest specific surface area and the pore size distribution is suitable for the rapid oxidation reaction. Such a favorable BET surface area and hierarchical pore distribution may be beneficial for the immersion of liquid electrolyte, accelerating ion diffusion and alleviating the structural strain during the electrochemical reaction. Furthermore, XRD

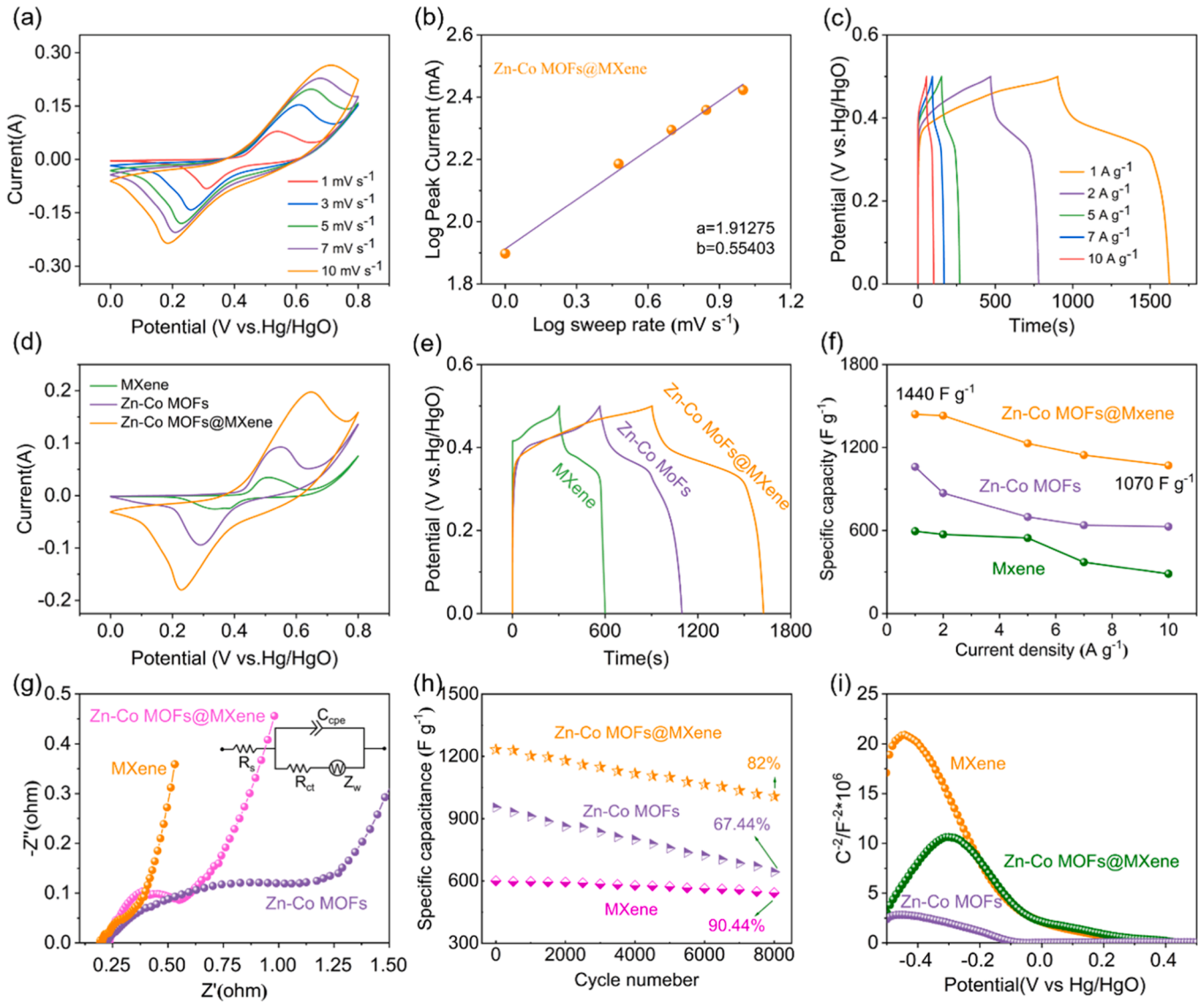

Fig. 5. (a) CV curves for Zn-Co MOFs@MXene at different scan rates from 1 to 10 mV s^{-1}, (b) calculation of the b-value during charge–discharge processes from the relationship between the sweep rate and peak current for Zn-Co MOFs@MXene, and (c) GCD curves for Zn-Co MOFs@MXene at different current densities. (d) CV curves under a scan rate of 5 mV s^{-1} with the potential range from 0 to 0.8 V, and (e) GCD curves at 1 A/g for MXene, Zn-Co MOFs, and Zn-Co MOFs@MXene samples. (f) The specific capacitances contrast of different samples with varied current densities. (g) EIS spectra, (h) the cycling performance at 5 A/g, and (i) the Mott-Schottky plots of MXene, Zn-Co MOFs, and Zn-Co MOFs@MXene samples.

analysis (Fig. 4f and Fig. S5) provides further evidence for the successful assembly of Co-Zn MOFs on MXene. The major diffraction peaks correspond to (002), (004), (104), and (110) crystal planes of MXene and (110), (211), (222), (431), and (541) crystal planes of ZIF-67, respectively.

The electrode material was coated with nickel foam with a loading of 5 mg/cm^2 and tested in a three-electrode test system using 1 M KOH electrolyte [39,40]. Fig. 5a and Fig. S6 present the cyclic voltammetry (CV) curves of MXene, Zn-Co MOFs, and Zn-Co MOFs@MXene at different scan rates. The shape of the voltammogram shows symmetric Faraday redox peaks, indicating an ideal capacitance behavior. A strong pair of redox peaks exist between 0 and 0.8 V (vs. Hg/HgO), proving that the charge storage is not only due to the rapid diffusion of OH^- at the electrode surface, but also most of all governed by Faraday redox reactions of Zn^{2+}/Zn^{3+} and Co^{2+}/Co^{3+} during the electrochemical process. The changes in the Zn and Co oxidation states provide active sites for electrochemical reactions, which is expected to improve the electrochemical performance. The relevant redox reactions of the electrochemical reaction can be described as follows:

$$xZn^{2+} + yCo^{2+} \leftrightarrow xZn^{3+} + yCo^{3+} + (x + y)\, e^-$$

As the scan rate (1–10 mV s^{-1}) increases, the enclosed region of the CV curve becomes more prominent, and the anodic and cathodic peaks shift toward positive and negative directions, respectively. The observed increase in anodic peak current density and decrease in cathode peak current density demonstrate a low resistance at the interface where the oxygen reduction reaction occurs. This indicates a rapid and reversible redox reaction of the active sites at the electrode-electrolyte interface. During the CV test, different voltage scan rates (v, mV/s) result in different peak current values (i, mA)[41]. By correlating the scan rate to the generated peak current response, it is possible to distinguish whether the capacitor's charging and discharging behavior is diffusive or pseudocapacitive in nature. Fig. 5b shows a linear relationship between the peak current and scan voltage, indicating a capacitance-controlled process. The charging/discharging of the electrode material can be described using Eqs. (1)–(3) in the Supplementary. The kinetic process between the electrolyte and the surface of the electrode material is an important indicator to measure the performance of the capacitor. Diffusion control is caused by redox reactions on the surface of the electrode, and surface control is deduced by adsorption/desorption of ions on the surface. For the electrode material, the value of b is calculated to be 0.554, indicating the redox process is consistent with diffusion-controlled behavior. In Fig. 5c, the galvanostatic charge/discharge (GCD) curves of the electrodes are shown at different current densities ranging from 1 to 10 A/g. The voltage-time curves exhibit nearly symmetrical behavior, indicating the excellent electrochemical performance of Zn-Co MOFs@MXene due to its high specific surface area derived from its layered structure. Moreover, the voltage plateau in GCD curves suggests the presence of a Faraday reaction process, consistent with the redox peak observed in the CV curve. A small loss of charge is unavoidable because during charging and discharging, the surface part of the material and a small portion near the surface are involved in an electrochemical reaction resulting in internal wear. The Faraday efficiency of the Zn-Co MOFs@MXene electrode is still about 85 % at a current density of 1 A/g. The area of the CV curve for the Zn-Co MOFs@MXene in Fig. 5d is significantly larger than that of the other two samples, indicating a higher capacitance. The introduction of MXene greatly improves the electrical conductivity of the material. This improvement can be attributed to MXene providing a larger specific surface area, offering an increased number of active sites for more redox reactions to occur. The presence of oxygen-containing groups on the MXene surface facilitates the formation of new surface states that combine with ions enabling a lower charge storage potential[42,43]. Ultimately, the layered structure of MXene provides a favorable pathway for ion migration, allowing for enhanced accessibility to ions in the electrolyte and providing more active sites for ions adsorption at the electrode during the charging and discharging process. At the same time, it avoids the "dead volume" associated with conventional adhesive polymer binders and conductive additives [44]. Fig. 5e presents the GCD curves of different electrode materials at a current density of 1 A/g. Each curve exhibits a distinct plateau during the charge/discharge process, indicating that the charge on the surface of the positive and negative collectors undergoes controlled accumulation and release without rapid voltage changes. This suggests that the charge participates in the redox reactions within the electrode materials rather than accumulating on the surface. Notably, Zn-Co MOFs@MXene shows the longest charge/discharge time, indicating a superior electrical capacity than the control samples. This excellent electrochemical performance can be attributed to the introduction of MXene, which facilitates the formation of a three-dimensional structure and electrically conductive network, which plays a vital role in the charging and discharging process. It is noteworthy that even at high current densities, Zn-Co MOFs@MXene maintains a significant charge/discharge plateau and longer charge/discharge time than Zn-Co MOFs, highlighting the effectiveness of MXene in improving the electrochemical performance.

In Fig. 5f, the capacitance values of each sample are presented at different current densities. At high current densities, limitations in the charge transfer capability of the material lead to a decrease in capacitance. However, at a current density of 1 A/g, Zn-Co MOFs@MXene exhibits a capacitance of 1440 F/g, which maintains at 1070 F/g even at a current density as high as 10 A/g. This represents a capacitance retention rate of up to 75 % for Zn-Co MOFs@MXene, significantly higher than the 59 % of pure Zn-Co MOFs. The substantial improvement in capacitance can be attributed to the conductive network established by MXene that provides fast ion and electron transfer channels, ensuring enhanced performance. The equivalent circuit model fitted by the Nyquist plot and the Bode phase angle diagram (Fig. 5g and Fig. S7) illustrated that the Zn-Co MOFs@MXene electrode possessed an Electrolyte solution (R_s =0.25 Ω) and charged transfer (R_{ct}=0.72 Ω) resistances, signifying its good charge transfer kinetics attributed to its good electrical property supported by its low sheet resistance. The intercept value of Zn-Co MOFs@MXene is smaller at higher frequencies compared to Zn-Co MOFs electrode, which indicates lower bulk charge transfer resistance. In addition, the diffusion impedance (Z_w) observed in the low-frequency range indicates that the diffusion resistance of Zn-Co MOFs@MXene is also lower. Moreover, Fig. 5h shows the excellent cycling stability of Zn-Co MOFs@MXene, with a capacitance retention of 82 % after 8000 cycles at 5 A/g. Fig. S8 shows the SEM images of the electrode material before and after cycling. Compared with the morphology of Zn-Co MOFs@MXene before cycling in Fig. S8a, nanoparticles at the surface of the laminar structure in Fig. S8b after cycling have some degree of agglomeration and the size is slightly increased. However, the overall structure remains almost unchanged, which indicates that the good stability of Zn-Co MOFs@MXene. This excellent cycling stability can be attributed to the laminar structure of Zn-Co MOFs@MXene, which provides sufficient space to efficiently accommodate volume changes during the reaction and effectively prevents the electrode material collapse. The Mott-Schottky plots, acquired at a frequency of 1 kHz, are shown in Fig. 5i. The Mott-Schottky curves exhibit similar shapes for different electrode materials within the − 0.5 V to 0.5 V potential sweep range. All Mott-Schottky plots show negative slopes, indicating that all samples can be classified as p-type semiconductors. According to Eq. (5) in the Supplementary, we can see that the carrier concentration is proportional to the absolute value of the slope in the graph: the larger the slope, the larger the carrier concentration.

To demonstrate the electrochemical performance of Zn-Co MOFs@MXene/NF in practical applications, a flexible all-solid-state hybrid supercapacitor (HSC) is assembled. The HSC configuration, illustrated in Fig. 6a, consists of Zn-Co MOFs@MXene/NF as the positive electrode, AC as the negative electrode, and PVA-KOH hydrogel as the

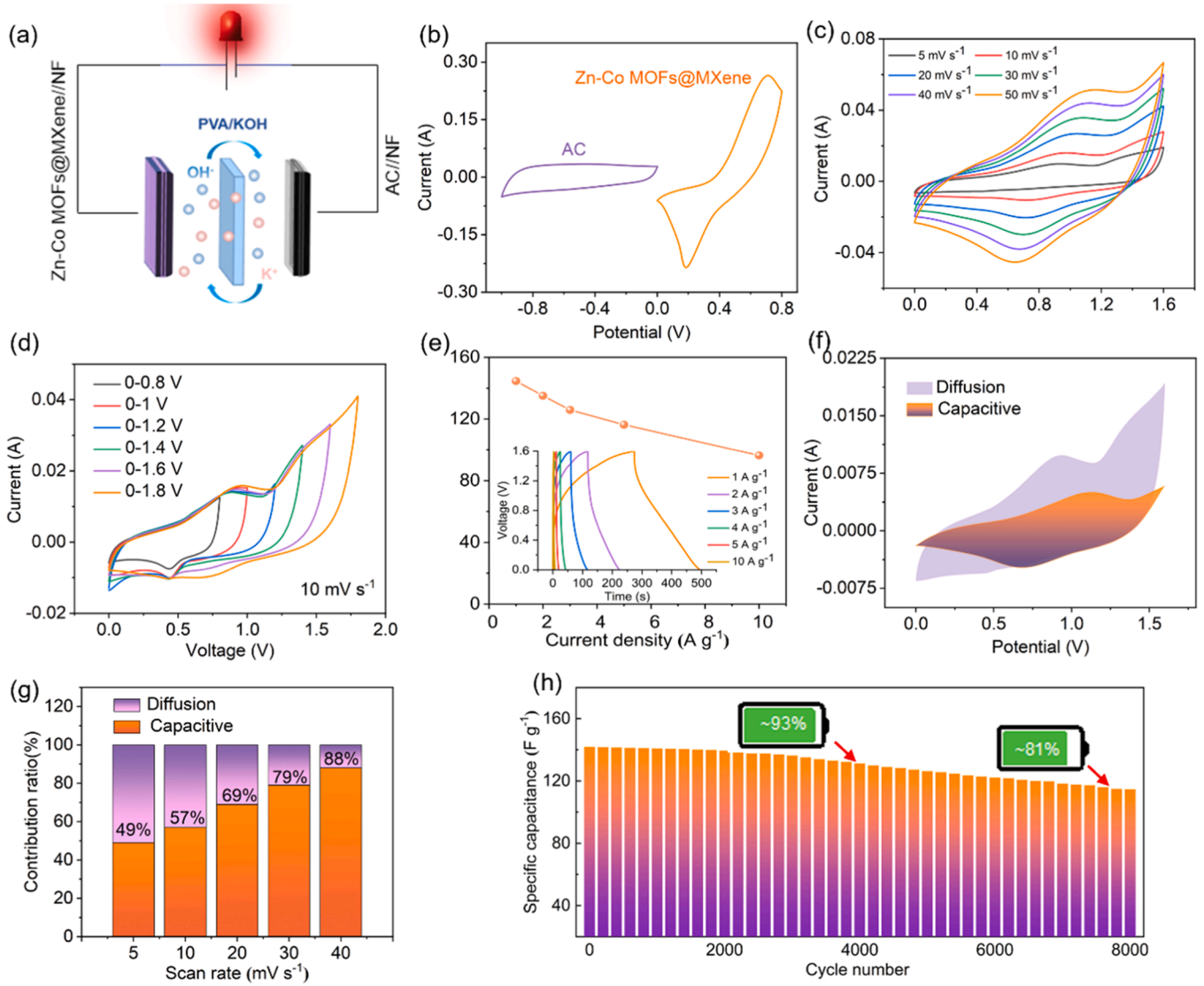

Fig. 6. (a) Schematic illustration of the HSC based on Zn-Co MOFs@MXene/NF as the positive electrode and AC//CF as the negative electrode, (b) CV curves of the AC//CF and Zn-Co MOFs@MXene/NF at 10 mV s^{-1} based on three electrode configurations, (c) CV curves of the as-assembled HSC with different scan rates in the voltage window of 0–1.6 V, (d) CV curves of the as-assembled HSC at 10 mV s^{-1} ranging from 0.8 to 1.8 V, (e) the specific capacitance values of the as-assembled hybrid supercapacitor and GCD curves of the as-assembled hybrid supercapacitor at different current densities, (f) the separation of capacitive and diffusion currents of the as-assembled hybrid supercapacitor at a sweep rate of 5 mV s^{-1}, (g) the contribution ratio of capacitive and diffusion controlled processes at different scan rates, and (h) stability and over 8000 cycles.

separator/electrolyte**.** It is crucial to maintain a charge balance (q+ = q-) between the cathode and anode during the assembly of the device. The loading amount of active substance on the negative and the positive electrodes is determined by Eqs. (6)–(8) in the Supplementary.

To evaluate the electrochemical performance of the AC negative electrode, rectangular CV curves and triangular GCD curves are typically used in a three-electrode configuration. Fig. S9 demonstrates the characteristics of electric double-layer capacitors (EDLC). As shown in Fig. 6b, the CV curve of activated carbon shows a subrectangular shape, indicating the dominance of bilayer capacitance in activated carbon. By combining its potential window of − 1 V to 0 V with that of the cathode material (0–0.8 V), the voltage window can effectively be expanded, resulting in a higher energy density. The mass loads of the positive and negative electrodes of the asymmetric device were 0.005 g and 0.016 g, respectively. The CV curve of the Zn-Co MOFs@MXene/AC device in Fig. 6c shows a closed loop for the operating voltage range of 0–1.6 V at different scan rates. Even at a high scan rate of 50 mV s^{-1}, the CV shape of the device is hardly distorted and still shows good energy storage performance and satisfactory electrochemical properties. The device, designed as a hybrid asymmetric supercapacitor, exhibits an undeformed CV shape, excellent stability, and fast reversible energy storage characteristics (Fig. 6d). These characteristics enable the scaling up of the device to 1.6 V. When the voltage is increased to 1.8 V, polarization occurs, primarily due to electrolyte decomposition at high voltages and the generations of bubbles during this process. This phenomenon hinders the practical use of the device. To strike a balance between maximum energy density and safe operating voltage, a voltage window of 0–1.6 V is determined as optimal for the two electrodes. Fig. 6e illustrates the GCD curves at different current densities. The charging and discharging curves show similar isosceles shapes, indicating that the charging and discharging capacitances are essentially the same, thus demonstrating excellent Coulomb efficiency. Additionally, the Zn-Co MOFs@MXene//AC device exhibits a specific capacitance of 144.7 F/g at 1 A/g, confirming its superior electrochemical performance. Fig. 6f reveals that the capacitive performance is about 49 % of the total charge stored at 5 mV s^{-1}, and this ratio increases with higher scan rates, as

depicted in Fig. 6g. At 40 mV s^{-1}, the capacitive contribution can reach 88 % confirming that a capacitive-based kinetics process determines the electrochemical performance. Furthermore, Fig. 6h demonstrates that the specific capacitance is maintained at 80.78 % after 8000 cycles at 1 A/g, highlighting the device's structural stability and excellent reversibility.

The development of high-performance flexible power supplies is crucial for the advancement of smart wearable electronics [1,45,46]. The inset in Fig. 7a demonstrates the excellent flexibility of our hybrid supercapacitor, as it can be easily bent and twisted to various angles. Importantly, no significant electrochemical performance changes are observed during the bending and twisting process, indicating the remarkable flexibility and mechanical stability of the assembled hybrid supercapacitor. This is further supported by the CV curves in Fig. 7b and the GCD curves at 1 A/g in Fig. 7c. Fig. S10a shows the CV curve of the device during the bending-releasing cycle. It can be seen that there are just small fluctuations when the state of folding and relaxation shifts, indicating the good mechanical properties and flexibility stability of the asymmetric supercapacitors. The fluctuation may be induced by the insufficient contact between lead electrodes and the device during bending cycles. After 1000 cycles, the CV curve in Fig. S10b is almost indistinguishable from that of Fig. S10a, confirming that the device maintains its electrochemical performance without loss in the periodic bending-releasing perturbation. The durability of this hybrid supercapacitor is further investigated under continuous bending from 0° to 180°, as shown in Fig. 7d. Fig. 7e shows that the Zn-Co MOFs@MXene//AC device achieves an excellent energy density of 51 Wh/kg at a power density of 1.59 kW/kg. Notably, the power density remains nearly constant at different current densities. Moreover, our assembled hybrid supercapacitors can quickly charge cell phones, which significantly broadens their application in specific situations and environments. Furthermore, by connecting four assembled hybrid supercapacitors in series, 44 LEDs can be easily lit as illustrated in Fig. 7f and Video 1–2. Above all, our flexible hybrid supercapacitor surpasses recent reports in terms of energy density, power density, cycling stability, and flexibility, as evidenced by results in Fig. 7g and Table S2.

Hydrogels possess remarkable stretchable and flexible properties, making them ideal for applications as piezoresistive sensors for pressure and curvature sensing. In particular, the PAM-BTO/NaCl composite organic films can withstand different deformations and multiple rounds

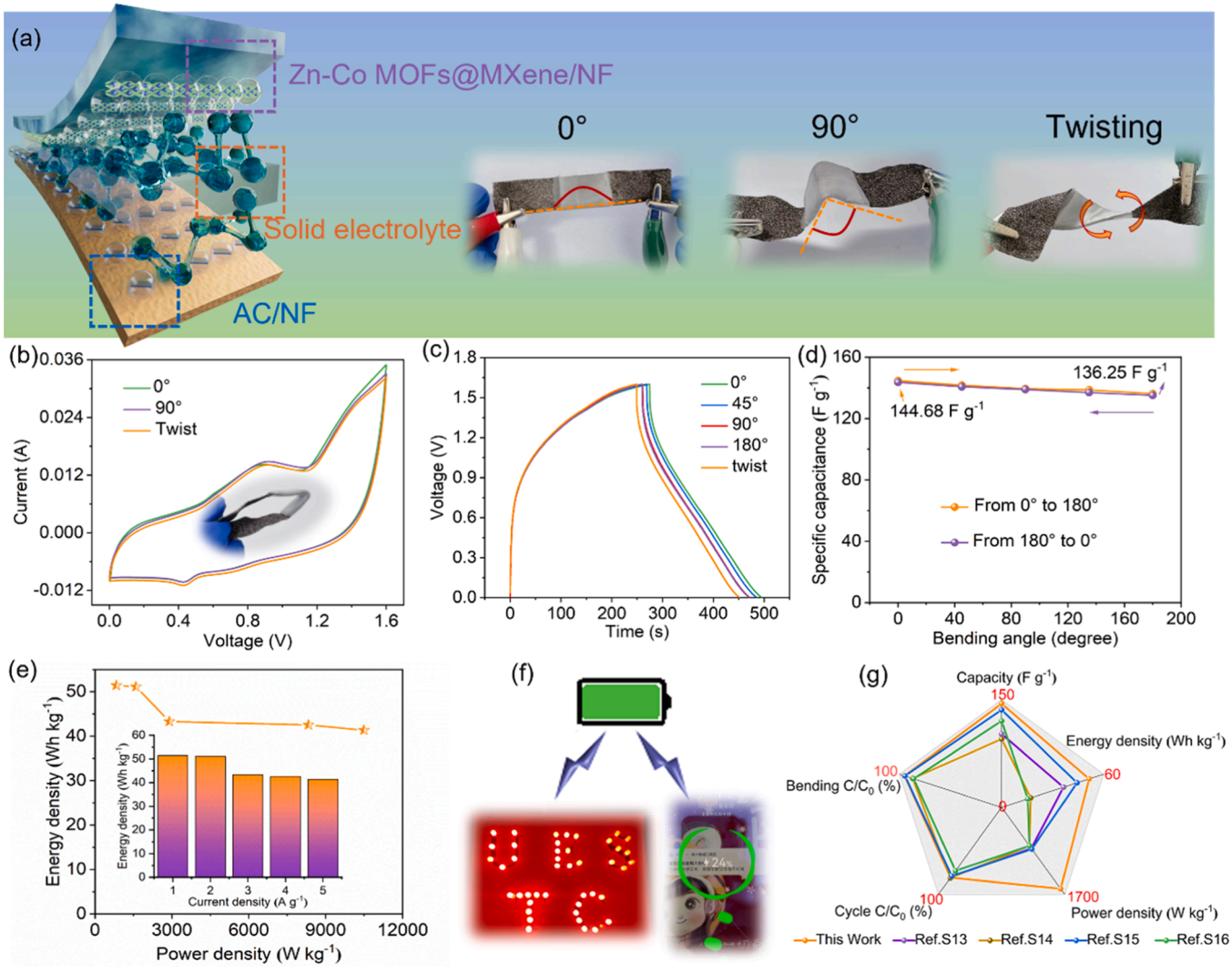

Fig. 7. (a) Schematic diagram of an all-solid-state flexible hybrid supercapacitor (consisting of Zn-Co MOFs@MXene as the positive electrode, AC as the negative electrode and KOH/PVA solid electrolyte in between) and optical photo of bending and folding (b) CV curves of the as-assembled hybrid supercapacitor at 10 mV s^{-1} under different bending and twisting angles, the inset shows a digital image of a hybrid supercapacitor bent to 90°; (c) GCD curves after bending at different angles; (d) the capacitance retention under different bending angles; (e) Ragone diagram of the assembled asymmetric device (The inset shows the energy density -current density performance graph); (f) The assembled solid-state supercapacitor is used to light up LEDs and charge cell phones; (g) A comparison between our hybrid supercapacitor and previous reported works.

of mechanical stretching, as depicted in Fig. 8a and b. These films can be uniaxially stretched up to 400 % within the 2–10 cm range. The hydrogel resistance changes during stretching and mechanical deformation, mainly due to changes in the 3D conductive interconnection network of the PAM polymer chains [47,48]. Moreover, the resistance change is further influenced by the polarization of BTO within the hydrogel under mechanical deformation [48]. In addition, introducing NaCl to hydrogels enhances their energy dissipation and toughens the material by inducing chain entanglement and increasing Young's modulus, thanks to the salt precipitation effect[7]. As shown in Fig. 8c, the relative resistance changes $\Delta R/R_0$ (ΔR is the resistance change with strain, and R_0 is the initial resistance before strain) exhibit a distinct step-like trend observed when an equiproportional progressive strain is applied to the hydrogel sensor. Notably, $\Delta R/R_0$ remains almost constant at the same tensile strain, and the resistance of the organic hydrogel exhibits a stable plateau during the holding strain, evidencing the excellent electromechanical stability of the organic hydrogel sensor. To further validate this characteristic, we provide visual evidence through the application of mechanical tensile stress (Video 3) and the corresponding brightness modulation of an LED. We further investigated the sensitivity of the organic hydrogel with increasing strain according to Eq. (11) in the Supplementary. Fig. 8d illustrates the linear increase in $\Delta R/R_0$, evidencing the sensitivity of the organic hydrogel. The gauge factor (GF) reaches 1.52 within the 0–400 % strain range. Notably, the PAM-BTO/NaCl organic hydrogel sensor shows an exponential dependence on the applied strain, with the GF increasing to 2.12 in the strain range of 400–600 %. This value surpasses that of previous reports (Table S3). Applying strain to the organic hydrogel sensor leads to significant changes in the resistance signal. The reasons for this may be attributed to two factors: (1) the strain-sensitivity of the organic hydrogel due to the release of large amounts of ions from the strong NaCl electrolyte. The absorbed ions, Na^+ and Cl^-, within the polymer chain network provide increased availability of dissociable ions [49–51]; (2) the external forces applied to the organic hydrogel sensor compresses its porous three-dimensional network structure leading to a reduction in the ion transport path. Mechanical stretching of the hydrogel significantly increases its length, resulting in a reduced cross-sectional area and thus an increase in the resistance of the organic hydrogel strain sensor [52,53]. Fig. 8e shows a series of cyclic stretches with constant strain to observe the relative resistance strain fluctuations. The time vs. $\Delta R/R_0$ response curves exhibit high linearity and repeatability. The self-healing behavior of the organic hydrogel can be observed in Video 4. When the thin film specimen is cut into two halves, the LED powered by the supercapacitor immediately turns off. However, upon rejoining the separated film, the LED regains its brightness instantly and maintains the same level. Over time at 40 °C, the hydrogel undergoes self-healing, where the polymer matrix is rearranged, and the interface fracture is repaired.

To achieve the goal of device integration, we connected the fabricated strain sensor in series with the supercapacitor and an ammeter to form a complete circuit. The supercapacitor was charged using a power source, and the integrated flexible sensor was powered by the charged supercapacitor (Fig. 9a). As shown in Fig. 9b, the current signal of the sensor exhibited steady and periodic signal variations as it was cyclically stretched and released at a constant strain of 20 %. Notably, the relative current variation ($\Delta I/I_0$; ΔI is the relative current variation with strain and I_0 is the initial current before strain) remained nearly constant during 50 loading cycles, as depicted in the inset. This shows the feasibility and durability of our supercapacitors as a substitute for conventional energy sources in driving wearable sensors. Fig. 9c

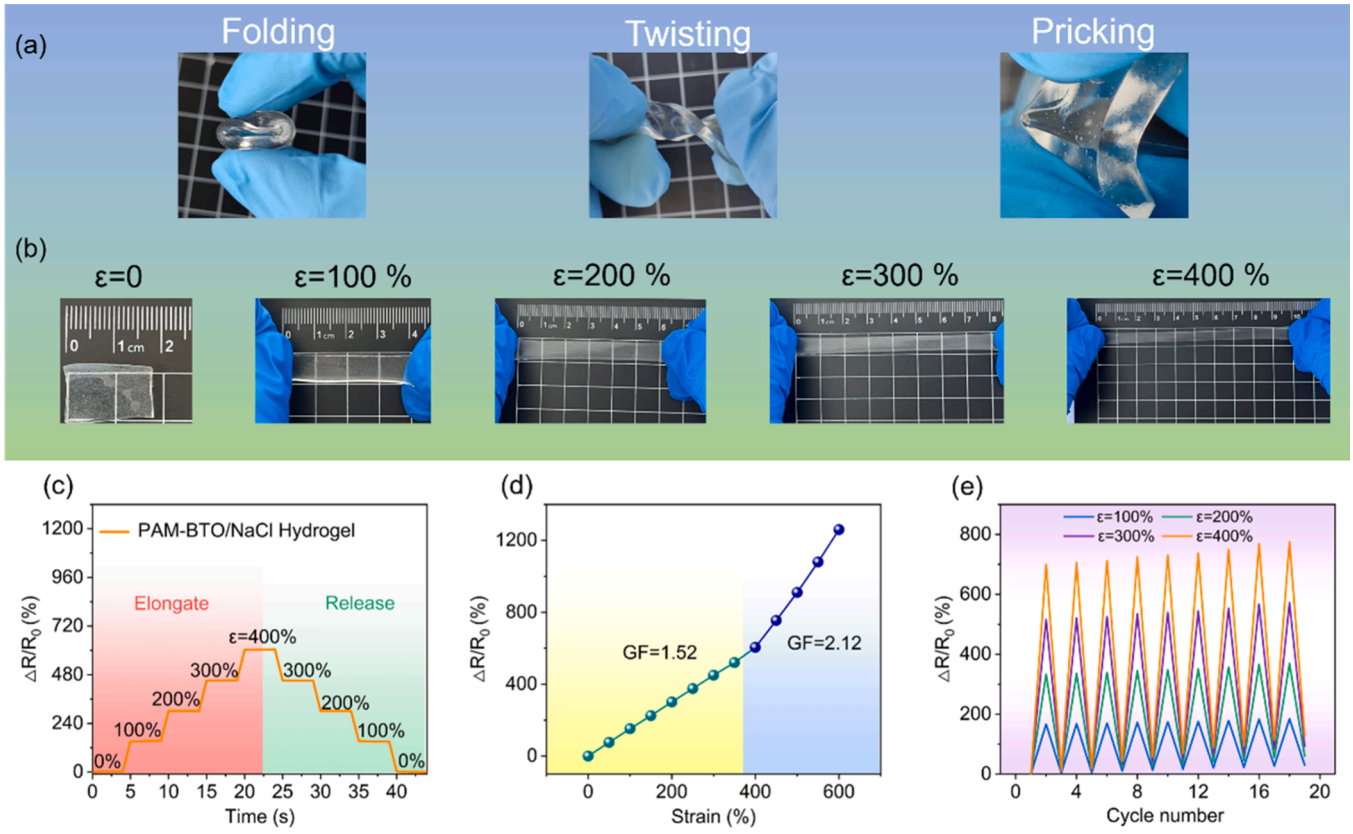

Fig. 8. (a) Optical images of the as-prepared PAM-BTO/NaCl hydrogel in different deformation states of folding, twisting, and stabbing with a scissor; (b) Photographs of the as-prepared PAM-BTO/NaCl composite hydrogel at the initial state and different mechanical stretched states; (c) Resistance response of the PAM-BTO/NaCl hydrogel strain sensor stretched to 100 %, 200 %, 300 %, and 400 %; (d) Relative resistance–strain response curves of the PAM-BTO/NaCl hydrogel strain sensor; (f) Resistance response of repeated stretching tests of the organic hydrogel strain sensor at different strains (100 %, 200 %, 300 %, and 400 %).

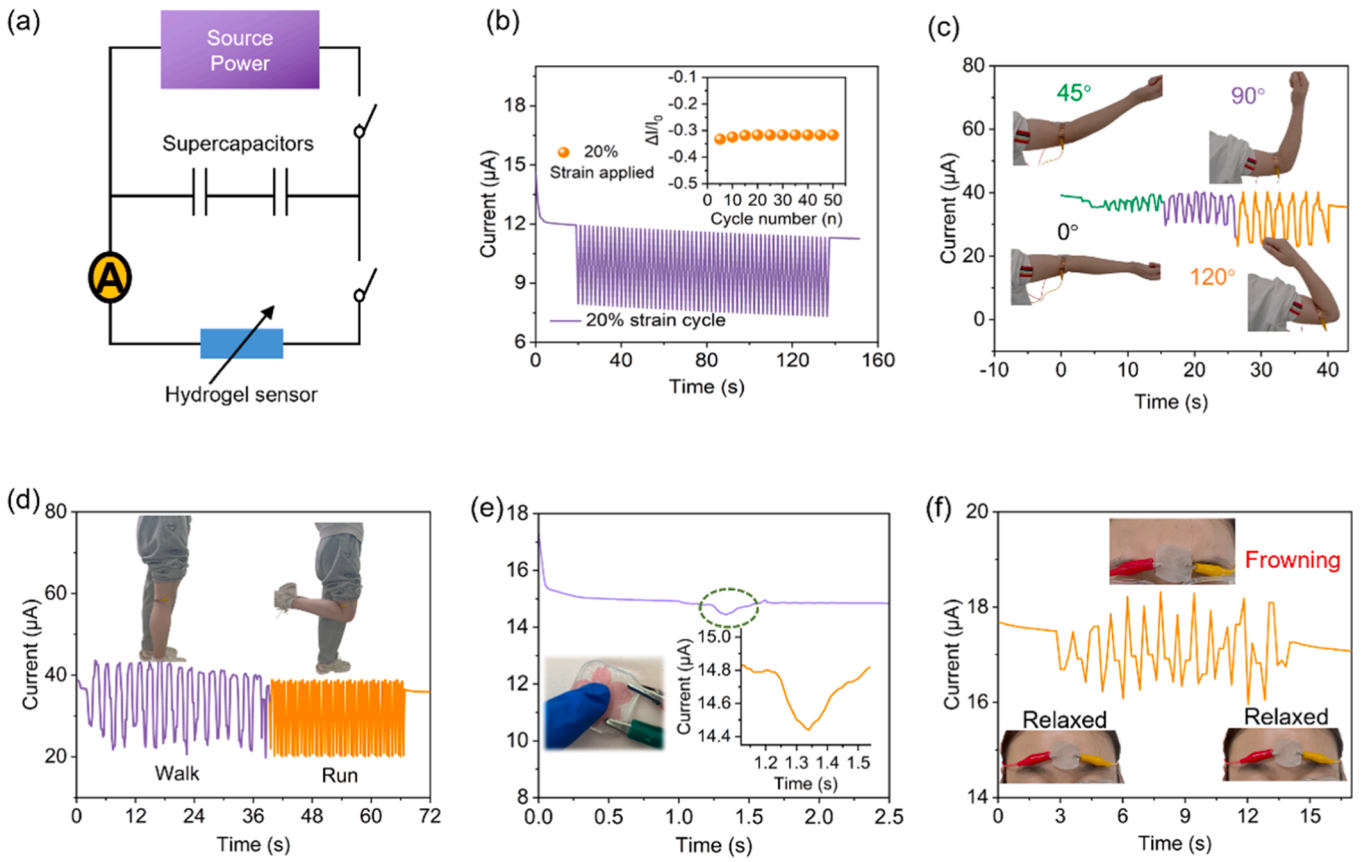

Fig. 9. (a) Circuit diagram for self-powered integrated system testing; (b) Time-current response curve of a strain sensor driven by a supercapacitor at 20 % applied strain for 50 cycles. The inset shows the relative current change ($\Delta I/I_0$); Digital images and corresponding time-current response curves of self-powered integrated systems in human motion monitoring: (c) arm movements, (d) walking and running, (e) touching (h) frowning.

demonstrates the detection of arm bending using the self-powered integrated system. As the arm is stretched, the connected strain sensor undergoes various degrees of stretching, resulting in an increased maximum current change with the bending angle ranging from 45° to 120°. The self-powered sensor exhibits a stable response during cyclic bending at a certain angle. The entire process, as shown in Video 5, showcases the capability of the self-powered wearable integrated system to detect mechanical strain in the arm through real-time data transmission to a cell phone app via wireless Bluetooth connectivity. Furthermore, Fig. 9d illustrates the sensor placement on the knee joint to monitor both low-frequency (walking) and high-frequency (running) motion processes. The self-driven integrated system detects changes in current response at different frequencies, enabling the detection of differential motion speed. These results show that the integrated system is able to discriminate between the same motion performed at different frequencies. The self-driven integrated system can also detect subtle motions such as touch (Fig. 9e), frown (Fig. 9f), and more, in addition to successfully monitoring large-scale motions. The device exhibits sensitivity to minor environmental changes and maintains stability in terms of current fluctuations, indicating excellent electromechanical stability. In conclusion, the organic hydrogel-based strain sensor, driven by a high-performance solid-state flexible supercapacitor, is capable of monitoring the full range of human motion.

3. Conclusions

We have successfully developed a self-driven smart sensor system consisting of flexible solid-state Zn-Co MOFs@MXene supercapacitors and PAM-BTO/NaCl organic ion hydrogel sensors. The solid-state supercapacitor demonstrates excellent energy density of 51 Wh/kg at a power density of 1.59 kW/kg. The assembled supercapacitor retains its remarkable mechanical flexibility even under different twisting and bending angles. After high-intensity bending, the organic ionic hydrogel strain sensor exhibits excellent sensing performance characterized by high sensitivity, high ductility, and electromechanical stability. The self-driven integrated system can be easily attached to a flexible substrate on human skin and realize functions such as real-time monitoring and testing through human-machine interaction. This advancement provides an effective idea for the future development of skin prostheses, human-robot interaction, and neuro-robotic technology research.

CRediT authorship contribution statement

Guo-Tao Xiang: Resource, Methodology, Writing – original draft, Formal analysis, Methodology, Visualization. **Na Chen:** Methodology. **Bin Lu:** Visualization. **Raul D. Rodriguez:** Writing – review & editing. **Evgeniya Sheremet:** Formal analysis. **Jia-Lei Xu:** Software. **Jin-Ju Chen:** Conceptualization, Supervision.

Declaration of Competing Interest

The authors declare that they have no known competing financial interests or personal relationships that could have appeared to influence the work reported in this paper.

Data availability

Data will be made available on request.

Acknowledgements

The work was supported by the Sichuan Science and Technology Program (grant No. 2023YFG0215) and Russian Science Foundation (grant No. 22-12-20027).

Appendix A. Supporting information

Supplementary data associated with this article can be found in the online version at doi:10.1016/j.nanoen.2023.108936.

References

[1] S. Gong, X. Zhang, X.A. Nguyen, Q. Shi, F. Lin, S. Chauhan, Z. Ge, W. Cheng, Hierarchically resistive skins as specific and multimetric on-throat wearable biosensors, Nat. Nanotechnol. (2023), https://doi.org/10.1038/s41565-023-01383-6.

[2] Z. Zhang, W. Wang, Y. Jiang, Y.X. Wang, Y. Wu, J.C. Lai, S. Niu, C. Xu, C.C. Shih, C. Wang, H. Yan, L. Galuska, N. Prine, H.C. Wu, D. Zhong, G. Chen, N. Matsuhisa, Y. Zheng, Z. Yu, Y. Wang, R. Dauskardt, X. Gu, J.B. Tok, Z. Bao, High-brightness all-polymer stretchable led with charge-trapping dilution, Nature 603 (7902) (2022) 624–630, https://doi.org/10.1038/s41586-022-04400-1.

[3] M. Wang, Y. Yang, J. Min, Y. Song, J. Tu, D. Mukasa, C. Ye, C. Xu, N. Heflin, J. S. McCune, T.K. Hsiai, Z. Li, W. Gao, A wearable electrochemical biosensor for the monitoring of metabolites and nutrients, Nat. Biomed. Eng. 6 (11) (2022) 1225–1235, https://doi.org/10.1038/s41551-022-00916-z.

[4] Z. Wei, J. Wang, Y. Liu, J. Yuan, T. Liu, G. Du, S. Zhu, S. Nie, Sustainable triboelectric materials for smart active sensing systems, Adv. Funct. Mater. 32 (52) (2022), https://doi.org/10.1002/adfm.202208277.

[5] D. Lu, T. Liu, X. Meng, B. Luo, J. Yuan, Y. Liu, S. Zhang, C. Cai, C. Gao, J. Wang, S. Wang, S. Nie, Wearable triboelectric visual sensors for tactile perception, Adv. Mater. 35 (7) (2023), 2209117, https://doi.org/10.1002/adma.202209117.

[6] H. Park, J.W. Kim, S.Y. Hong, G. Lee, H. Lee, C. Song, K. Keum, Y.R. Jeong, S. W. Jin, D.S. Kim, J.S. Ha, Dynamically stretchable supercapacitor for powering an integrated biosensor in an all-in-one textile system, ACS Nano 13 (9) (2019) 10469–10480, https://doi.org/10.1021/acsnano.9b04340.

[7] J. Huang, S. Peng, J. Gu, G. Chen, J. Gao, J. Zhang, L. Hou, X. Yang, X. Jiang, L. Guan, Self-powered integrated system of a strain sensor and flexible all-solid-state supercapacitor by using a high performance ionic organohydrogel, Mater. Horiz. 7 (8) (2020) 2085–2096, https://doi.org/10.1039/d0mh00100g.

[8] Y. Zhang, J. Wu, S. Zhang, N. Shang, X. Zhao, S.M. Alshehri, T. Ahamad, Y. Yamauchi, X. Xu, Y. Bando, MOF-on-MOF nanoarchitectures for selectively functionalized nitrogen-doped carbon-graphitic carbon/carbon nanotubes heterostructure with high capacitive deionization performance, Nano Energy 97 (2022), https://doi.org/10.1016/j.nanoen.2022.107146.

[9] Y. Lee, V.K. Bandari, Z. Li, M. Medina-Sanchez, M.F. Maitz, D. Karnaushenko, M. V. Tsurkan, D.D. Karnaushenko, O.G. Schmidt, Nano-biosupercapacitors enable autarkic sensor operation in blood, Nat. Commun. 12 (1) (2021), 4967, https://doi.org/10.1038/s41467-021-24863-6.

[10] H. Ma, F. Lv, L. Shen, K. Yang, Y. Jiang, J. Ma, X. Geng, T. Sun, Y. Pan, Z. Xie, M. Xue, N. Zhu, Self-healing all-in-one energy storage for flexible self-powering ammonia smartsensors, Energy Environ. Mater. 5 (3) (2021) 986–995, https://doi.org/10.1002/eem2.12227.

[11] W. Wang, L. Xu, L. Zhang, A. Zhang, J. Zhang, Self-powered integrated sensing system with in-plane micro-supercapacitors for wearable electronics, Small (2023), e2207723, https://doi.org/10.1002/smll.202207723.

[12] H. Li, S. Chang, M. Li, K. Hou, L. Han, A. Cao, H. Li, Y. Shang, Flexible and stable carbon nanotube film strain sensors with self-derived integrated electrodes, ACS Appl. Mater. Interfaces 13 (46) (2021) 55600–55610, https://doi.org/10.1021/acsami.1c13530.

[13] Q. Wang, J. Liu, X. Ran, D. Zhang, G. Shen, M. Miao, High-performance flexible self-powered strain sensor based on carbon nanotube/ZnSe/$CoSe_2$ nanocomposite film electrodes, Nano Res. 15 (1) (2021) 170–178, https://doi.org/10.1007/s12274-021-3453-5.

[14] Y. Zhao, B. Zhang, B. Yao, Y. Qiu, Z. Peng, Y. Zhang, Y. Alsaid, I. Frenkel, K. Youssef, Q. Pei, X. He, Hierarchically structured stretchable conductive hydrogels for high-performance wearable strain sensors and supercapacitors, Matter 3 (4) (2020) 1196–1210, https://doi.org/10.1016/j.matt.2020.08.024.

[15] X. Ren, M. Li, L. Qiu, X. Guo, F. Tian, G. Han, W. Yang, Y. Yu, Cationic vacancies and interface engineering on crystalline–amorphous gamma-phase Ni–Co oxyhydroxides achieve ultrahigh mass/areal/volumetric energy density flexible all-solid-state asymmetric supercapacitor, J. Mater. Chem. A 11 (11) (2023) 5754–5765, https://doi.org/10.1039/d2ta09035j.

[16] G. Xiang, J. Yin, G. Qu, P. Sun, P. Hou, J. Huang, X. Xu, Construction of $ZnCo_2S_4$@$Ni(OH)_2$ core–shell nanostructures for asymmetric supercapacitors with high energy densities, Inorg. Chem. Front. 6 (8) (2019) 2135–2141, https://doi.org/10.1039/c9qi00653b.

[17] G. Xiang, Y. Meng, G. Qu, J. Yin, B. Teng, Q. Wei, X. Xu, Dual-functional $NiCo_2S_4$ polyhedral architecture with superior electrochemical performance for supercapacitors and lithium-ion batteries, Sci. Bull. 65 (6) (2020) 443–451, https://doi.org/10.1016/j.scib.2020.01.004.

[18] B. Li, M. Yu, Z. Li, C. Yu, H. Wang, Q. Li, Constructing flexible all-solid-state supercapacitors from 3D nanosheets active bricks via 3D manufacturing technology: a perspective review, Adv. Funct. Mater. 32 (29) (2022), https://doi.org/10.1002/adfm.202201166.

[19] J. Wang, W. Guo, Z. Liu, Q. Zhang, Engineering of self-aggregation-resistant MnO_2 heterostructure with a built-in field for enhanced high-mass-loading energy storage, Adv. Energy Mater. (2023), https://doi.org/10.1002/aenm.202300224.

[20] C. Liu, H. Wu, X. Wang, J. Fan, H. Su, D. Yang, Y. Wei, F. Du, Y. Dall'Agnese, Y. Gao, Flexible solid-state supercapacitor integrated by methanesulfonic acid/polyvinyl acetate hydrogel and Ti_3C_2T, Energy Stor. Mater. 54 (2023) 164–171, https://doi.org/10.1016/j.ensm.2022.09.037.

[21] Y. Ma, H. Sheng, W. Dou, Q. Su, J. Zhou, E. Xie, W. Lan, Fe_2O_3 nanoparticles anchored on the $Ti_3C_2T_x$ MXene paper for flexible supercapacitors with ultrahigh volumetric capacitance, ACS Appl. Mater. Interfaces 12 (37) (2020) 41410–41418, https://doi.org/10.1021/acsami.0c11034.

[22] Y. Yang, D. Zhang, Y. Liu, L. Shen, T. Zhu, X. Xu, J. Zheng, X. Gong, Solid-state double-network hydrogel redox electrolytes for high-performance flexible supercapacitors, ACS Appl. Mater. Interfaces 13 (29) (2021) 34168–34177, https://doi.org/10.1021/acsami.1c06980.

[23] Y. Qian, Y. Yu, W. Wu, Q. Fan, C. Chai, J. Hao, Wide-temperature flexible supercapacitor from an organohydrogel electrolyte and its combined electrode, Chem. Eur. J. 29 (25) (2023), e202300123, https://doi.org/10.1002/chem.202300123.

[24] L. Wang, Y. Tang, Y. Li, C. Liu, N. Wei, W. Zeng, D. Liang, Multifunctional integrated interdigital microsupercapacitors and self-powered iontronic tactile pressure sensor for wearable electronics, ACS Appl. Mater. Interfaces 14 (41) (2022) 47136–47147, https://doi.org/10.1021/acsami.2c15117.

[25] Y. Yuan, J. Zhou, G. Lu, J. Sun, L. Tang, Highly stretchable, transparent, and self-adhesive ionic conductor for high-performance flexible sensors, ACS Appl. Polym. Mater. 3 (3) (2021) 1610–1617, https://doi.org/10.1021/acsapm.0c01442.

[26] W. Cui, Y. Zheng, R. Zhu, Q. Mu, X. Wang, Z. Wang, S. Liu, M. Li, R. Ran, Strong tough conductive hydrogels via the synergy of ion-induced cross-linking and salting-out, Adv. Funct. Mater. 32 (39) (2022), https://doi.org/10.1002/adfm.202204823.

[27] Q. Wang, J. Liu, G. Tian, D. Zhang, Co@n-cnt/mxenes in situ grown on carbon nanotube film for multifunctional sensors and flexible supercapacitors, Nanoscale 13 (34) (2021) 14460–14468, https://doi.org/10.1039/d1nr03641f.

[28] M.S. Kim, J.W. Kim, J. Yun, Y.R. Jeong, S.W. Jin, G. Lee, H. Lee, D.S. Kim, K. Keum, J.S. Ha, A rationally designed flexible self-healing system with a high performance supercapacitor for powering an integrated multifunctional sensor, Appl. Surf. Sci. 515 (2020), https://doi.org/10.1016/j.apsusc.2020.146018.

[29] Y. Lu, K. Jiang, D. Chen, G. Shen, Wearable sweat monitoring system with integrated micro-supercapacitors, Nano Energy 58 (2019) 624–632, https://doi.org/10.1016/j.nanoen.2019.01.084.

[30] S. Pu, Z. Wang, Y. Xie, J. Fan, Z. Xu, Y. Wang, H. He, X. Zhang, W. Yang, H. Zhang, Origin and regulation of self-discharge in MXene supercapacitors, Adv. Funct. Mater. 33 (8) (2022), https://doi.org/10.1002/adfm.202208715.

[31] L. Song, C. Dai, X. Jin, Y. Xiao, Y. Han, Y. Wang, X. Zhang, X. Li, S. Zhang, J. Zhang, Y. Zhao, Z. Zhang, L. Qu, Pure aqueous planar microsupercapacitors with ultrahigh energy density under wide temperature ranges, Adv. Funct. Mater. 32 (30) (2022), https://doi.org/10.1002/adfm.202203270.

[32] J.-Q. Qi, C.-C. Zhang, H. Liu, L. Zhu, Y.-W. Sui, X.-J. Feng, W.-Q. Wei, H. Zhang, P. Cao, MXene-wrapped $ZnCo_2S_4$ core–shell nanospheres via electrostatic self-assembly as positive electrode materials for asymmetric supercapacitors, Rare Met. 41 (8) (2022) 2633–2644, https://doi.org/10.1007/s12598-021-01956-1.

[33] J. Zhou, B. Liu, L. Zhang, Q. Li, C. Xu, H. Liu, MXene-driven in situ construction of hollow core-shelled $Co_3V_2O_8$@$Ti_3C_2T_x$ nanospheres for high-performance all-solid-state asymmetric supercapacitors, J. Mater. Chem. A 10 (46) (2022) 24896–24904, https://doi.org/10.1039/d2ta06579g.

[34] J. Fu, L. Li, J.M. Yun, D. Lee, B.K. Ryu, K.H. Kim, Two-dimensional titanium carbide (MXene)-wrapped sisal-like $NiCo_2S_4$ as positive electrode for high-performance hybrid pouch-type asymmetric supercapacitor, Chem. Eng. J. 375 (2019), https://doi.org/10.1016/j.cej.2019.121939.

[35] J.-Q. Qi, M.-Y. Huang, C.-Y. Ruan, D.-D. Zhu, L. Zhu, F.-X. Wei, Y.-W. Sui, Q.-K. Meng, Construction of $CoNi_2S_4$ nanocubes interlinked by few-layer $Ti_3C_2T_x$ mxene with high performance for asymmetric supercapacitors, Rare Met. 41 (12) (2022) 4116–4126, https://doi.org/10.1007/s12598-022-02167-y.

[36] L. Yue, L. Chen, X. Wang, D. Lu, W. Zhou, D. Shen, Q. Yang, S. Xiao, Y. Li, Ni/Co-MOF@aminated MXene hierarchical electrodes for high-stability supercapacitors, Chem. Eng. J. 451 (2023), https://doi.org/10.1016/j.cej.2022.138687.

[37] Y. Wei, W. Luo, X. Li, Z. Lin, C. Hou, M. Ma, J. Ding, T. Li, Y. Ma, PANI-MnO_2 and $Ti_3C_2T_x$ (MXene) as electrodes for high-performance flexible asymmetric supercapacitors, Electrochim. Acta 406 (2022), https://doi.org/10.1016/j.electacta.2022.139874.

[38] Q. Jiang, N. Kurra, M. Alhabeb, Y. Gogotsi, H.N. Alshareef, All pseudocapacitive MXene-RuO_2 asymmetric supercapacitors, Adv. Energy Mater. 8 (13) (2018), https://doi.org/10.1002/aenm.201703043.

[39] L. Fan, Z. Hou, T. Liu, X. Liang, A. Ivanets, K. Ma, X. Su, Fe-NX-C material with excellent supercapacitor performance prepared through oleic acid acidification pretreatment—oily sludge pyrolysis process, J. Environ. Chem. Eng. 10 (5) (2022), https://doi.org/10.1016/j.jece.2022.108256.

[40] A. Pramanik, S. Maiti, T. Dhawa, M. Sreemany, S. Mahanty, High faradaic charge storage in $ZnCo_2S_4$ film on Ni-foam with a hetero-dimensional microstructure for hybrid supercapacitor, Mater. Today Energy 9 (2018) 416–427, https://doi.org/10.1016/j.mtener.2018.07.007.

[41] Q.-C. Jia, H.-J. Zhang, L.-B. Kong, Nanostructure-modified in-situ synthesis of nitrogen-doped porous carbon microspheres (NPCM) loaded with $FeTe_2$ nanocrystals and NPCM as superior anodes to construct high-performance lithium-ion capacitors, Electrochim. Acta 337 (2020), https://doi.org/10.1016/j.electacta.2020.135749.

[42] W. He, G. Zhao, P. Sun, P. Hou, L. Zhu, T. Wang, L. Li, X. Xu, T. Zhai, Construction of longan–like hybrid structures by anchoring Nickel hydroxide on yolk–shell polypyrrole for asymmetric supercapacitors, Nano Energy 56 (2019) 207–215, https://doi.org/10.1016/j.nanoen.2018.11.048.

[43] M.Q. Zhao, X. Xie, C.E. Ren, T. Makaryan, B. Anasori, G. Wang, Y. Gogotsi, Hollow MXene spheres and 3D macroporous mxene frameworks for Na-ion storage, Adv. Mater. 29 (37) (2017), https://doi.org/10.1002/adma.201702410.

[44] P. Sun, N. Li, C. Wang, J. Yin, G. Zhao, P. Hou, X. Xu, Nickel-cobalt based aqueous flexible solid state supercapacitors with high energy density by controllable surface modification, J. Power Sources 427 (2019) 56–61, https://doi.org/10.1016/j.jpowsour.2019.04.062.

[45] S. Shen, J. Yi, Z. Sun, Z. Guo, T. He, L. Ma, H. Li, J. Fu, C. Lee, Z.L. Wang, Human machine interface with wearable electronics using biodegradable triboelectric films for calligraphy practice and correction, Nanomicro Lett. 14 (1) (2022), 225, https://doi.org/10.1007/s40820-022-00965-8.

[46] T. Cui, Y. Qiao, D. Li, X. Huang, L. Yang, A. Yan, Z. Chen, J. Xu, X. Tan, J. Jian, Z. Li, S. Ji, H. Liu, Y. Yang, X. Zhang, T.-L. Ren, Multifunctional, breathable MXene-PU mesh electronic skin for wearable intelligent 12-lead ECG monitoring system, Chem. Eng. J. 455 (2023), https://doi.org/10.1016/j.cej.2022.140690.

[47] Y. Wang, L. Zhang, A. Lu, Highly stretchable, transparent cellulose/PVA composite hydrogel for multiple sensing and triboelectric nanogenerators, J. Mater. Chem. A 8 (28) (2020) 13935–13941, https://doi.org/10.1039/d0ta02010a.

[48] Z. Wang, Z. Liu, G. Zhao, Z. Zhang, X. Zhao, X. Wan, Y. Zhang, Z.L. Wang, L. Li, Stretchable unsymmetrical piezoelectric $BaTiO_3$ composite hydrogel for triboelectric nanogenerators and multimodal sensors, ACS Nano 16 (1) (2022) 1661–1670, https://doi.org/10.1021/acsnano.1c10678.

[49] G. Chen, J. Huang, J. Gu, S. Peng, X. Xiang, K. Chen, X. Yang, L. Guan, X. Jiang, L. Hou, Highly tough supramolecular double network hydrogel electrolytes for an artificial flexible and low-temperature tolerant sensor, J. Mater. Chem. A 8 (14) (2020) 6776–6784, https://doi.org/10.1039/d0ta00002g.

[50] H. Zou, X. Meng, X. Zhao, J. Qiu, Hofmeister effect-enhanced hydration chemistry of hydrogel for high-efficiency solar-driven interfacial desalination, Adv. Mater. 35 (5) (2023), e2207262, https://doi.org/10.1002/adma.202207262.

[51] S.-N. Li, X.-F. He, Z.-F. Zeng, B. Jiang, Q. Wu, L.-X. Gong, Y. Li, J. Bae, S. Wang, L.-C. Tang, Mechanically ductile, ionically conductive and low-temperature tolerant hydrogel enabled by high-concentration saline towards flexible strain sensor, Nano Energy 103 (2022), https://doi.org/10.1016/j.nanoen.2022.107789.

[52] B. Zheng, H. Zhou, Z. Wang, Y. Gao, G. Zhao, H. Zhang, X. Jin, H. Liu, Z. Qin, W. Chen, A. Ma, W. Zhao, Y. Wu, Fishing Net-inspired mutiscale ionic organohydrogels with outstanding mechanical robustness for flexible electronic devices, Adv. Funct. Mater. (2023), https://doi.org/10.1002/adfm.202213501.

[53] Y. Wang, D. Xiao, L. Quan, H. Chai, X. Sui, B. Wang, H. Xu, Z. Mao, Mussel-inspired adhesive gelatin-polyacrylamide hydrogel wound dressing loaded with tetracycline hydrochloride to enhance complete skin regeneration, Soft Matter 18 (3) (2022) 662–674, https://doi.org/10.1039/d1sm01373d.